Nanotubes Complexed with DNA and Proteins for Resistive-Pulse Sensing

Jingjie Sha,[†,‡] Tawfique Hasan,[§] Silvia Milana,[§] Cristina Bertulli,[‡] Nicholas A. W. Bell,[‡] Giulia Privitera,[§] Zhonghua Ni,[†] Yunfei Chen,[†] Francesco Bonaccorso,[§,⊥] Andrea C. Ferrari,[§] Ulrich F. Keyser,[‡,*] and Yan Yan S. Huang[‡,∥,*]

[†]School of Mechanical Engineering, Southeast University, Nanjing 210096, China, [‡]Cavendish Laboratory, University of Cambridge, Cambridge CB3 0HE, United Kingdom, [§]Cambridge Graphene Centre, University of Cambridge, Cambridge CB3 0FA, United Kingdom, [⊥]CNR-IPCF, Istituto per i Processi Chimico-Fisici, Messina 98158, Italy, and [∥]Department of Chemical Engineering and Institute of Biotechnology, University of Cambridge, Cambridge CB2 1QT, United Kingdom

ABSTRACT We use a resistive-pulse technique to analyze molecular hybrids of single-wall carbon nanotubes (SWNTs) wrapped in either single-stranded DNA or protein. Electric fields confined in a glass capillary nanopore allow us to probe the physical size and surface properties of molecular hybrids at the single-molecule level. We find that the translocation duration of a macromolecular hybrid is determined by its hydrodynamic size and solution mobility. The event current reveals the effects of ion exclusion by the rod-shaped hybrids and possible effects due to temporary polarization of the SWNT core. Our results pave the way to direct sensing of small DNA or protein molecules in a large unmodified solid-state nanopore by using nanofilaments as carriers.

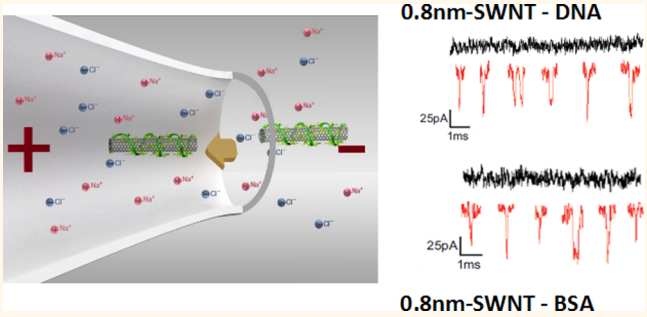

KEYWORDS: nanotubes · DNA · proteins · nanopore · hybrids · sensors

The molecular combination of organic and inorganic nanomaterials has led to developments of functional hybrids.[1−7] These have applications in solar cells,[1] superconductors,[2] bioelectronics,[3,4,8] and medical diagnostics,[5−7,9] just to name a few examples. In particular, systems based on the combination of water-soluble biomolecules and colloidal nanomaterials have been intensively investigated, such that versatile functionalities can be tailor-designed by tuning the surface chemistry of the two components for integration with biology.[10−12] In some cases, strong interaction affinity is already present between the pristine forms of the two constituents, thus facilitating highly stable hybrids. For example, it is possible to assemble macromolecular hybrids based on single-wall carbon nanotubes (SWNTs) and a variety of biomolecules, such as viruses,[1] deoxyribonucleic acid (DNA),[13] lipids,[14] and proteins.[9,15] Studies also reported spontaneous unfolding and attachment of biomolecules onto SWNTs.[16−19]

The architecture of individual hybrids, as well as their intermolecular aggregation, plays a crucial role in device performance.[1] To develop devices with novel functions, it is therefore necessary to access their molecular structure on a single-molecule level. Current technique facilitating direct structural characterization often relies on visualization of the hybrids using high-resolution microscopic techniques.[16,20,21] This requires deposition and fixing of the hybrids on a surface. However, such a methodology diminishes many important attributes of hybrid complexes in solution. These attributes, which include the formation of electric double layers[22] and the dynamic aggregation behavior,[19] are key to many potential applications of these functional hybrids.[5,6,10,23]

Advances in solid-state nanopore technology[24] have significantly progressed the field of single-molecule sizing in solution.[24−26] Information on the conformation of individual molecules during translocation can be extrapolated through a resistive pulse "read-out" of the ionic current through the nanopore.[27] This technique was employed to study DNA folding[28] and to analyze the translocation of a wide range of biomolecules.[29] However, most,

* Address correspondence to yysh2@cam.ac.uk, ufk20@cam.ac.uk.

Received for review June 29, 2013 and accepted September 25, 2013.

Published online September 25, 2013
10.1021/nn403323k

but not all,[24−26,30] have been organic and monolithic molecules.[31] Reference 32 has shown the translocation of SWNTs wrapped with $(AC)_{15}$ (*i.e.*, single-strand DNA oligomers of 15 repeated units of adenine and cytosine) through silicon nitride nanopores. This suggests the use of solid-state nanopores as a structural characterization tool for organic−inorganic colloidal hybrids.

To explore the potential of using the versatile capillary-based nanopores[33] for molecular hybrid sensing, we investigate the translocation characteristics of SWNT−biomolecule hybrids, with different sizes and surface properties. SWNT−biomolecule hybrids are prepared using (6,5)-enriched CoMoCAT SWNTs (diameters of ∼0.8 nm) and arc-discharge SWNTs (diameter of ∼1.5 nm). These two commercially available SWNTs with distinct diameter ranges were chosen to ensure that the results are not specific to a particular SWNT choice. We design four hybrids by noncovalent functionalization between SWNTs and biomolecules. For the surface binding, DNA oligomer $(AC)_{15}$ is chosen because it represents a large group of short single-stranded DNA (ssDNA) that cannot be detected in large conventional, bare solid-state nanopores.[34] Detection would only be made feasible by reducing the nanopore membrane thickness to below 10 nm, for example, as demonstrated by the technical advance by ref 35. It is thus of interest to evaluate whether using SWNTs as "carriers" of multiple, well-organized oligomers can amplify the detection signals in nanocapillaries,[33] which can be fabricated using widely available glass capillaries with short processing times and a high degree of controllability. We also consider SWNT and bovine serum albumin (BSA) hybrids (SWNT−BSA) because BSA is a common and well-characterized model blood serum protein,[36,37] and the hybrids have good biocompatibility,[9,38] demonstrating potential uses for biotechnology.[38−40] Following the characterization of the hybrids using conventional microscopy and spectroscopy techniques, we perform our translocation experiments using a nanocapillary setup. Our results show that the ionic current characteristics of translocation can reflect the cross-section thickness of the hybrids with subnanometer resolution.

RESULTS

Four SWNT−biomolecular hybrids with different combination of geometries and surface properties are produced. For the convenience of notation, the SWNTs will be represented using their mean diameters. We therefore label the samples as 1.5d-AC, 1.5d-AC-6hr, 0.8d-AC, 0.8d-BSA. The prefix indicates the modal diameter of the SWNT core, where P2 has a modal diameter of 1.5 nm and CoMoCAT has a modal diameter of 0.8 nm as confirmed by the results below. The second part of the label indicates the biomolecule coating. The third part, if present, indicates the duration of the sonication which differs from our standard preparation period of 2 h.

We believe that detailed characterization of the SWNT hybrids is necessary for the interpretation of the results generated by nanocapillary detection. Attributes such as the geometry, charge, and zeta-potential[34] of a translocating object are the well-recognized general considerations, which determine the resistive pulse read-out. We therefore employ atomic force microscopy (AFM) and zeta-potential measurements to determine these attributes. For the SWNT-based hybrids, specifically, we adopt Raman spectroscopy to measure the diameter distribution and the conduction characteristics of the SWNT cores. The dispersion qualities of the hybrids are further validated by photoluminescence spectroscopy (PLE). In-depth analysis of Raman and photoluminescence spectral signals reveal significant doping of the SWNTs by the biomolecules, which underlies the strong binding essential for utilizing SWNTs as a molecular carrier. Following the characterization process, our result analysis is dedicated to the translocation of SWNT hybrids through a nanocapillary. We focus on understanding how the event durations and currents of translocation can reflect the physical characteristics of the hybrids in an aqueous solution.

Solution Characteristics of Biomolecule−SWNT Hybrids. *Raman Spectroscopy*. Raman spectroscopy is a fast, powerful, and nondestructive method for characterization of carbon materials.[41,42] A number of important parameters, such as diameter, chirality, conduction character, orientation, doping, *etc.*, can be obtained from Raman characterization of SWNTs. Hence, Raman spectroscopy was employed to measure both the raw SWNT powders and the deposited SWNT−biomolecule hybrids, shown in Figure 1.

First, in the low-frequency region of the Raman spectra of SWNTs, radial breathing modes (RBMs)[43] are observed (Figure 1a,c,e,g). Their position, Pos(RBM), is inversely related to the SWNT diameter, d,[44−46] as given by the following: $\mathrm{Pos(RBM)} = (C_1/d) + C_2$.[44] A variety of C_1 and C_2 were proposed for this relation.[43−45,47] Here we use $C_1 = 214.4\ \mathrm{cm^{-1}}$ nm and $C_2 = 18.7\ \mathrm{cm^{-1}}$ from ref 44 because these were derived by plotting the SWNT resonance energies as a function of inverse RBM frequency, without any additional assumptions. Matching the diameter given by Pos(RBM) with excitation wavelength in the "Kataura plot"[48] also gives information on the semiconducting (s-SWNTs) or metallic (m-SWNTs) character. The G^+ and G^- bands are typically located in the $1500-1600\ \mathrm{cm^{-1}}$ region.[49,50] In s-SWNTs, they originate from the longitudinal (LO) and tangential (TO) modes, respectively, derived from the splitting of the E_{2g} phonon of graphene.[49,51] In m-SWNTs, the assignment of the G^+ and G^- bands is the opposite, and the fwhm of the G^- peak, fwhm(G^-), is larger, and Pos(G^-) down-shifted with respect to the semiconducting counterpart.[49,51] Doping could also modify the positions and fwhm values.[52,53] In m-SWNTs, a Pos(G^-) blue shift,

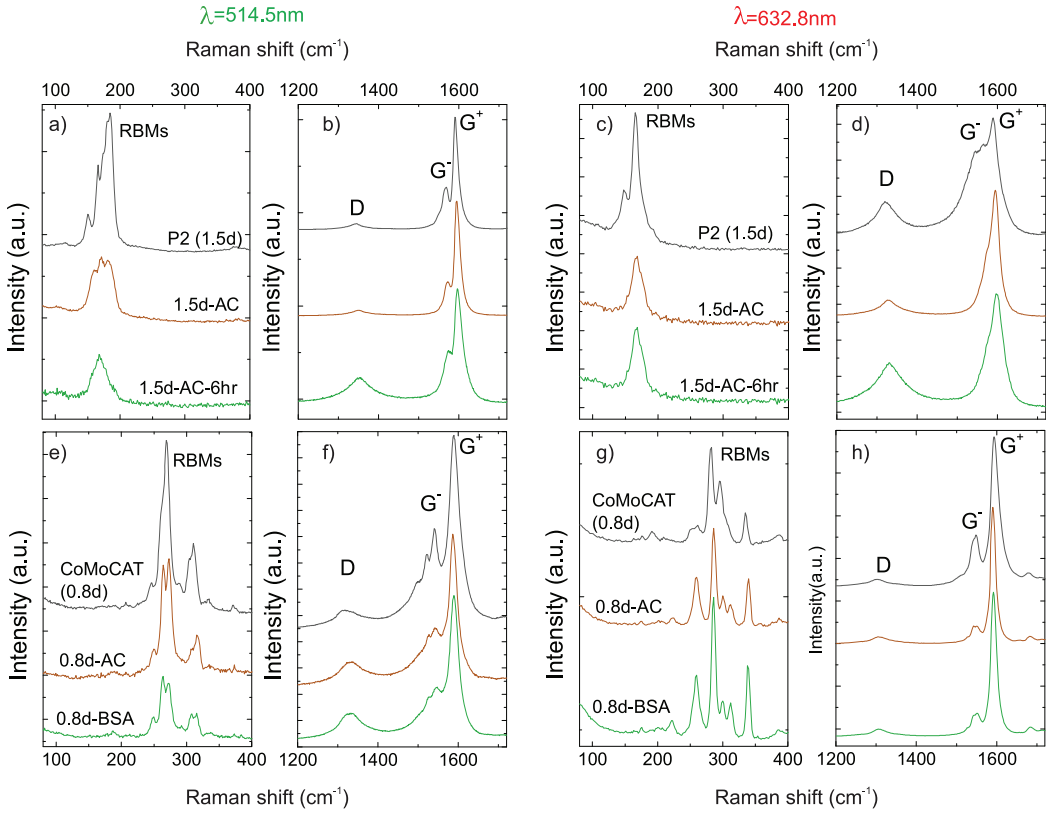

Figure 1. RBM and G band regions of SWNT powders and SWNT−biomolecule hybrids at laser excitations of 514.5 nm (a,b,e,f) and 632.8 nm (c,d,g,h) .

accompanied by a fwhm(G^-) decrease, is observed with electron or hole doping.[52,53] In s-SWNTs, doping up-shifts Pos(G^+) but does not affect fwhm(G^+).[52,53] Raman spectroscopy also probes possible damage *via* the D peak.[42,54,55] In the following, the RBM, G and D band features of the hybrids are discussed, first on the P2(1.5d) group and then on the CoMoCAT(0.8d) group.

For the P2(1.5d) group, the RBM region at 514.5 nm excitation (black line in Figure 1a) shows peaks ranging from ∼146 to ∼185 cm^{-1}, corresponding to a diameter of 1.29−1.68 nm.[44] The majority of the detected tubes are s-SWNTs because they are in resonance with this excitation wavelength.[44,48] In the G peak region (Figure 1b), evidence of splitting of the G^- peak is seen in all spectra. The peak at lower wavenumbers (∼1557 cm^{-1} in the 1.5d sample), due to LO mode of m-SWNTs[49] with a diameter of ∼1.0−1.1 nm,[49] blue shifts both for the 1.5d-AC (1568 cm^{-1}) and the 1.5d-AC-6hr (1563 cm^{-1}) with respect to the 1.5d one. Moreover, fwhm(G^-) is narrower both in the 1.5d-AC (∼5%) and 1.5d-AC-6hr (∼50%) spectra with respect to the 1.5d (fwhm(G^-) = 20.7 cm^{-1}). The peak at ∼1567 cm^{-1}, due to a combination of LO of m-SWNTs with a diameter of ∼1.4 nm[49] and TO of s-SWNTs with a diameter of ∼1.2 nm,[49] is blue-shifted (∼5 and ∼7 cm^{-1}) and narrower (∼14 and ∼58%) in the 1.5d-AC and 1.5d-AC-6hr spectra, respectively, compared to the corresponding peaks of the 1.5d sample. This change in the G^- peak region could be related to a different metallic or semiconducting nature of the tubes or to a different diameter distribution.[49] However, they show similar RBM features and no particular enrichment of m- and/or s-SWNTs (Figure 1a). Moreover, the difference in diameter is very small (0.08 nm) and not compatible with such blue shift and decrease of fwhm(G^-) for both LO and TO modes.[52,53] Thus, we infer that doping, likely due to SWNT−biomolecule charge transfer,[5] plays a role.[52,53] The presence of doping is also confirmed by the ∼4 and ∼3 cm^{-1} blue shift of Pos(G^+) in the 1.5d-AC and 1.5d-AC-6hr spectra, respectively, compared to 1.5d powder (Pos(G^+) ∼ 1592 cm^{-1}). We also note an increase of I(D)/I(G) from ∼0.05 to ∼0.25 in both 1.5d and 1.5d-AC. The increase in the D peak could be associated with the sonication time (6 h) that could damage the SWNTs.[56,57]

The spectra measured at 632.8 nm show effects similar to those from 514.5 nm excitation (Figure 1c,d). The spectrum of 1.5d in the RBM region is dominated by peaks from ∼146 to ∼178 cm^{-1} corresponding to 1.34−1.68 nm diameter.[44] In the G region (Figure 1d), the peak at ∼1550 cm^{-1} is up-shifted for both 1.5d-AC (∼8 cm^{-1}) and 1.5d-AC-6hr (∼10 cm^{-1}) with respect to 1.5d. There is also a ∼40 and ∼10% fwhm reduction for 1.5d-AC and 1.5d-AC-6hr, respectively, compared to 1.5d. The peak at ∼1570 cm^{-1} is blue-shifted ∼5 cm^{-1} for both samples, with respect to the starting material.

Finally, Pos(G^+) of 1.5d-AC and 1.5d-AC-6hr is also blue-shifted ~2 and ~4 cm^{-1}, respectively. These confirm the presence of doping[50,58] due to the wrapping of AC and that this effect increases slightly with the sonication time. Also, we note an increase of I(D)/I(G) in 1.5d-AC-6hr with respect to both 1.5d and 1.5d-AC, from ~0.33 to ~0.5.

We then turn our focus to the CoMoCAT (0.8d) group. The RBM region at 514.5 nm excitation for the CoMoCAT (0.8d) starting material (black line in Figure 1e) has peaks from ~207 to ~370 cm^{-1}, corresponding to a diameter range of 0.61−1.14 nm.[44] The majority of the detected tubes are m-SWNTs, with the ones having RBMs above 300 cm^{-1} being s-SWNTs.[44,48] Although a blue shift of Pos(G^-) and Pos(G^+) is detected in the Raman spectra of 0.8d-AC and 0.8d-BSA with respect to the starting material, fwhm(G^-) increases, while fwhm(G^+) decreases. This could be connected with the presence of m-SWNTs.[49] Moreover, I(G^+)/I(G^-) increases in 0.8d-AC and 0.8d-BSA, with respect to the starting material, another evidence of doping.[52]

The RBM region at 632.8 nm for the 0.8d indicates the presence of s-SWNTs since this wavelength is expected to be in resonance mostly with the second excitonic transition of 0.8d (CoMoCAT) s-SWNTs.[59] In the starting material (black line in Figure 1g), we detect peaks ranging from ~174 to ~385 cm^{-1} with a diameter distribution in the 0.58−1.38 nm range.[44,48] However, the peaks at ~282 and ~295 cm^{-1} corresponding to (7,5) and (8,3), respectively, are the most intense. s-SWNTs are also mainly detected in 0.8d-AC (red line in Figure 1g) and 0.8d-BSA (green line in Figure 1g).

In the G peak region (Figure 1h), evidence of splitting of the ~1550 cm^{-1} peak, due to LO of m-SWNTs and TO of s-SWNTs,[49] is seen. We fit the G peak with four Lorentzians (LO and TO of m-SWNTs and s-SWNTs). Small diameter (<0.6 nm) m-SWNTs contribute to the LO ~1515 cm^{-1} of the starting material.[49] For both 0.8d-AC and 0.8d-BSA (red line and green lines, respectively, in Figure 1h), there is a frequency increase (~10−12 cm^{-1}) with respect to the 0.8d sample. Moreover, I(G^+)/I(G^-) increases in 0.8d-AC and 0.8d-BSA, with respect to the starting material, which we take as evidence of doping.[52,53]

Based on the above analysis, Raman measurements indicate doping[52,53] in 1.5d-AC, 1.5d-AC-6hr, 0.8d-AC, and 0.8d-BSA. They also show a diameter distribution ranging from 1.29 to 1.68 nm for 1.5d and from 0.58 to 1.38 nm for 0.8d. Thus, the 0.8d samples have a larger diameter distribution with respect to 1.5d.

Photoluminescence Spectroscopy. s-SWNTs have a direct band gap. Therefore, photoluminescence (PL) from the isolated s-SWNTs due to exciton recombination is expected.[60] Photoluminescence excitation spectroscopy (PLE) is now one of the most common techniques to monitor SWNT dispersions.[59,61−66] In PLE, the (eh_{ii}, eh_{11}) resonances (where i = 1,2, ..., *etc.*) from different SWNTs appear as sharp features at (λ_{ex},λ_{em}), where λ_{ex} and λ_{em} are the excitation and emission wavelengths, respectively. Other peaks can also be observed in PLE, either due to excitonic phonon sidebands,[67−69] exciton energy transfer (EET),[59,61,62,70−72] or bright phonon sidebands (BS) of dark K-momentum excitons.[73] In particular, EET occurs *via* Förster resonance energy transfer between SWNTs in close proximity,[61,62] such as in bundles when eh_{ii} excitation of large band gap donor nanotubes induces emission from eh_{11} of a smaller band gap acceptor.[61,62] EET can thus identify the presence of small bundles.[59,63−66] The presence of m-SWNTs in large bundles can strongly quench the luminescence from s-SWNTs.[74] Therefore, PL is not observed in large SWNT bundles.[74] We thus use PLE to detect isolated tubes and small bundles in SWNT−biomolecule dispersions. This is crucial for the biomolecule translocation study through nanopores, as individualization of SWNTs increases the charge to mass ratio of the hybrids, hence, increasing their driving force. This consequently increases the probability of translocation.

Note that uncoated SWNTs, with their hydrophobic surface, form bundles and may still be present in the dispersions due to the 15 000*g* centrifugation we use here (which indeed were confirmed by AFM analysis shown later). Such level of centrifugal force ensures the presence of sufficient SWNTs to enable the observation of translocation events. However, the presence of m-SWNTs in these bundles will strongly quench the luminescence from s-SWNTs.[74] Therefore, PL will only be observed from isolated tubes or small bundles wrapped and stabilized by the biomolecules. Emission from large diameter (~1.5 nm) P2 SWNTs (present in the 1.5d-AC and 1.5d-AC-6hr hybrids), with lowest excitonic transition energy eh_{11} > 1600 nm,[75,76] is not observed due to strong absorption from water[77] and low sensitivity of our detector in this wavelength region.[59] In contrast, strong emission is seen from the (6,5)-enriched CoMoCAT SWNT hybrids (0.8d-AC and 0.8d-BSA) due to their smaller diameter, with an associated emission range of 900−1100 nm.[75,76] The corresponding PLE maps are shown in Figure 2a,b, where the SWNT chiralities giving rise to the high intensity emissions from (eh_{22}, eh_{11}) resonances are also indicated.[60,75,76] The strong (eh_{22}, eh_{11}) emission (571 nm, 993 nm) from (6,5) and their phonon sideband at (516 nm, 993 nm) is a signature of isolated small diameter SWNTs that are coated with biomolecules.[61,62] Other weaker (eh_{22}, eh_{11}) features present are due to isolated (6,4), (8,3), and (7,5) in 0.8d-BSA and (8,3), (7,5), (7,6), and (8,4) in 0.8d-AC. In addition to the key features assigned to the isolated SWNTs, one also observes EET features due to small SWNT bundles. For the 0.8d-AC in Figure 2a, the bands (571 nm, 1042 nm), (571 nm, 1124 nm), (993, 671) are assigned to EET[61,62] from (6,5) to (7,5), (6,5) to (8,4), and (8,3) to (6,5). For the 0.8d-BSA in Figure 2b, the band at (669 nm, 993 nm) is due

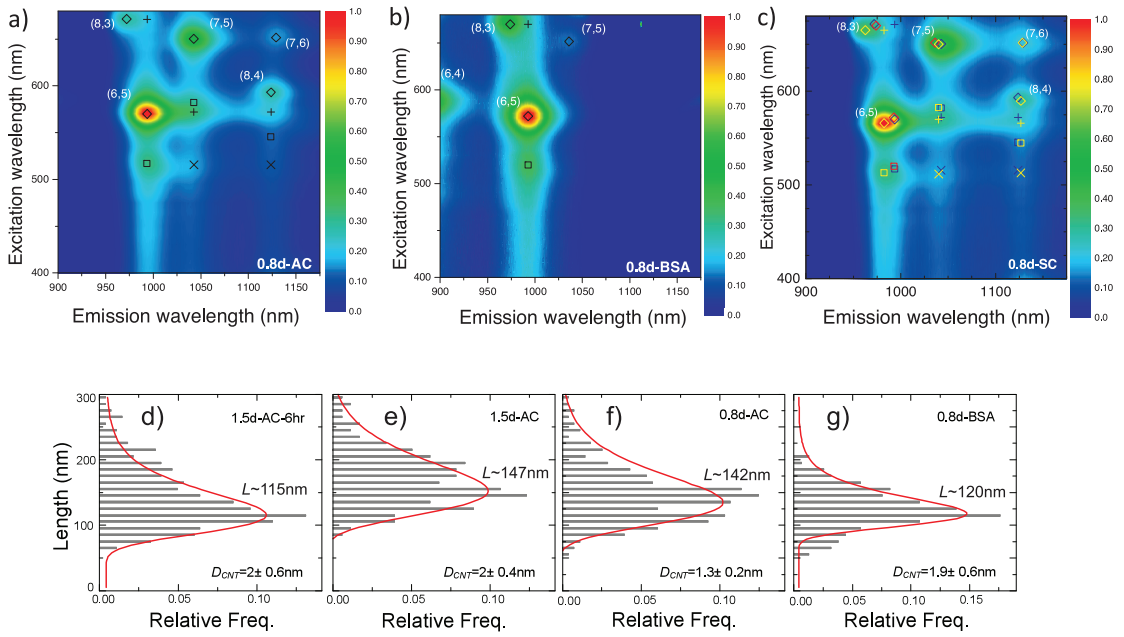

Figure 2. Photoluminescence maps of (a) 0.8d-AC, (b) 0.8d-BSA hybrids. (c) Comparison of the PLE contour of 0.8d-AC and 0.8d-BSA hybrids to the 0.8d dispersed using SC. Each (eh_{22},eh_{11}) resonance is labeled with the chiral index of the corresponding SWNT and is denoted by open ◊. The open □, solid + and × represent phonon sidebands, EET, and EET between sidebands of donors and excitons of acceptor nanotubes in small bundles, respectively. In (c), the yellow, blue, and red symbols denote positions of optical signatures from SC, AC, and BSA dispersed nanotubes, respectively. Histograms of lengths of the SWNT−biomolecule hybrids measured by AFM for (d) 1.5d-AC-6hr, (e) 1.5d-AC, (f) 0.8d-AC, and (g) 0.8d-BSA; the average height D_{cnt} of each hybrid is also indicated.

to EET from (8,3) to (6,5). We also observe EET from sidebands of (6,5) to (7,5) and (8,4) in 0.8d-AC.

Further, we also compare the PL emission from nanotubes in the SWNT−biomolecule dispersions with a 0.8d control sample dispersed in water with SC (sodium cholate surfactant), following the same procedure used for the biomolecule conjugation (Figure.2c). The optical signatures of (6,5) and (8,3) in 0.8d-AC and 0.8d-BSA are red-shifted ~10 meV with respect to the SC control sample. On the other hand, (7,5), (7,6), and (8,4) do not exhibit any noticeable shifts. Such large shifts in emission wavelength were also observed by ref 5 in PLE measurements of virus-wrapped SWNTs. The shifts are likely due to increased doping through SWNT−biomolecule charge transfer,[78] consistent with the Raman analysis above. The larger shifts in emission wavelength for the smaller diameter tubes are further enhanced by the change in surrounding dielectric environment due to their preferential wrapping and isolation by the biomolecules. In particular, BSA shows a strong preference of isolating smaller diameter SWNTs, as observed by strong emission from isolated (6,4), (6,5), and (8,3), coupled with weak or no emission from larger diameter SWNTs. In addition to doping and preferential isolation of small diameter nanotubes, PLE thus confirms the presence of isolated SWNTs and small bundles both of which are ideal candidates for translocation through the nanopores.

Atomic Force Microscopy. Following the spectroscopic methods for determining the nature of the SWNT core, AFM was performed to measure the physical sizes of the dried, SWNTs and hybrids deposited on substrates First, the diameters of the bare, unfunctionalized SWNTs (dispersed in *N*-methyl-2-pyrrolidone) are determined by AFM height measurements and found to be ~0.75−0.95 and ~1.3−1.9 nm for CoMoCAT and P2 SWNTs, respectively. These compare well with Raman spectroscopy (*i.e.*, 0.6−1.37 and 1.29−1.68 nm for CoMoCAT and P2 SWNTs, respectively). In all, both spectroscopy and microscopy measurements confirm that bare CoMoCAT SWNTs (mean diameter ~0.8 nm) have negligible overlap in diameter distribution compared to bare P2 SWNTs (mean diameter ~1.5 nm).

We then determine the size of the dehydrated SWNT−biomolecule hybrids in Figure 2d−g. Typical AFM images are presented in the Supporting Information. It is noted that the structure of the biomolecule-wrapped SWNTs has previously been evaluated by computational simulation, for example, for BSA-wrapped SWNTs[79] and DNA-wrapped SWNTs.[80] These studies both demonstrated the wrapping of SWNTs in the hydrophobic core of the biomolecules. 0.8d-AC is measured to have a mean diameter of 1.3 nm (standard deviation = 0.2 nm), implying an $(AC)_{15}$ coating thickness of ~0.25 nm, assuming a homogeneous layer. This $(AC)_{15}$ layer thickness is similar to that previously reported in ref 20 for the same hybrid. The measured mean diameter of ~2 nm for 1.5d-AC (standard deviation = 0.4 nm) and 1.5d-AC-6hr (standard deviation = 0.6 nm) is consistent

TABLE 1. Properties of SWNT–Biomolecule Conjugates Determined by Zetasizing Measurements, Calculated Based on Scattering from Spherical Objects

sample name	zeta-potential (mV)	zeta deviation (mV)	R_z (nm)	polydispersity index	$M_{complex}$, mobility (μm·cm/V·s)	mobility deviation (μm·cm/V·s)	$R_z/M_{complex}$ (SI unit)	$R_z/(M_{complex}\cdot E)$ (s)
1.5d-AC-6hr	−27.4	69.2	222.9	0.56	−2.1	5.4	10.4	1.0×10^{-5}
1.5d-AC	−22.0	85.8	187.1	0.58	−1.7	6.7	10.8	1.1×10^{-5}
0.8d-AC	−25.6	56.0	91.8	0.47	−2.0	4.4	4.6	4.6×10^{-6}
0.8d-BSA	−17.7	66.9	151.2	0.41	−1.4	5.2	10.9	1.1×10^{-5}

with the fact that the $(AC)_{15}$ thickness is ~0.25 nm, similar to that of 0.8d-AC. On the other hand, 0.8d-BSA shows a mean diameter of ~1.9 nm (standard deviation = 0.6 nm), indicating that the BSA layer contributes an additional ~1.1 nm. Reference 81 calculated that polypeptides in BSA assumed an unfolded configuration with their single twist of α-helix wrapping the nanotube surface. High-resolution AFM studies on BSA-coated double-wall nanotubes[21] showed that unfolded BSA molecules are present in localized regions along the tube length. Since an α-helix has a diameter of ~1.2 nm,[82] an average additional thickness of 1.1 nm is reasonable within measurement errors. Thus, the measured 1.9 nm mean diameter in 0.8d-BSA is within the expected range.

The length statistics of the SWNT–biomolecule hybrids are also indicated in Figure 2. It is found that the modal length of 1.5d-AC is 147 nm, and that of 0.8d-AC is 142 nm. That of 0.8d-BSA is 120 nm, even if sonication-treated for the same period. With a further 4 h sonication (6 h in total), the modal length of 1.5d-AC-6hr is reduced to 115 nm. Sonication cutting is a known effect during dispersion of nanotubes.[56,83]

Electric Charge and Zeta-Potential. Zeta-potential quantifies the electric potential in the interfacial double layer through which colloidal stability is defined.[84] The zeta-potentials of the hybrids are qualitatively determined using a Marlvern Zetasizer Nano range. This dynamic light scattering system measures the colloidal electrophoretic mobilities, that is, the ability of charges to move in a solution in response to an electric field.[84] Based on this empirical data, Table 1 summarizes the average hydrodynamic sizes (R_z, measured in nm), zeta-potentials (measured in mV), and electrophoretic mobilities (in μm·cm/V·s), of which values are calculated by considering light scattering from spherical objects (therefore, they act as approximation to our rod-shaped hybrids studied here). The average hydrodynamic sizes (*z*-average, R_z) for the 1.5d hybrids are greater than that of the 0.8d hybrids. Note that the ranking of R_z among the four hybrids differs from that measured by AFM in the dried hybrid lengths. This could be due to the additional charge screening lengths associated with the molecular wrapping around the SWNTs in solution. Although the measured zeta-potentials are all negative, as expected for the biomolecular coatings at pH 8,[85,86] the variation of the values is significant in 0.5 M NaCl. Due to the large deviation in zeta-potential, the mobilities calculated also show significant deviation. The correlation between the nanopore translocation and the Zetasizer measurements will be further elucidated in the next section.

Nanocapillary Detection. Resistive pulse sensing was performed in a nanocapillary configuration.[33] Figure 3a shows the setup which consists of a glass nanocapillary linking the *cis*- and *trans*-chambers of salt solutions. The nanocapillary terminal which faces the *cis*-chamber converges to a nanometer-sized aperture or "nanopore", where translocation of hybrids is detected. We perform translocation studies by adding an aliquot of analyte solution (~1/10 of the volume of the reservoir salt solution) in the *cis*-chamber (see Methods). At ±300 mV, our control studies of molecule-free salt solution and $(AC)_{15}$ show stable ionic current traces with similar root-mean-square noise levels, $I_{rms} < 4$ pA at 10 kHz. For BSA molecules, an increase in "noise" is observed at +300 mV, which may imply the passage of BSA molecules. However, no well-defined events could be recorded. For each of the biomolecule–SWNT hybrids, translocation events are observed when a positive potential is applied by the electrode inside the capillary. This is consistent with the negative zeta-potential of the hybrids determined by Zetasizer, though it differs from ref 32, which showed reversal translocation of $(AC)_{15}$–SWNT hybrids in a 1 M NaCl solution. Since the screening becomes increasingly dominant at high salt concentration, with greater zeta-potential variation, it is possible that a net positive electrophoretic mobility dominates at 1 M NaCl. Figure 3b displays typical current traces for each biomolecule–SWNT hybrid. When an event occurs, a sharp decrease in current (ΔI) is observed, indicating the exclusion of ions, by the physical volume of the hybrid. The current subsequently returns to the baseline level I_B after a duration Δt as the hybrid leaves the pore vicinity.

Event Dwell Time Δt. Studying Δt and the event current ΔI can reveal rich information on the conformation and structure of the translocating molecule. Figure 4a shows typical scatter plots of translocation characteristics, ΔI *versus* Δt, for all hybrids. The corresponding histogram analyses are plotted alongside in Figure 4b,c. These plots seem to only exhibit one cluster, some having a "tail" extending to longer Δt ranges. However, over 80% of the event population has durations shorter than 0.5 ms for each sample. We therefore consider the events which lie in the tail

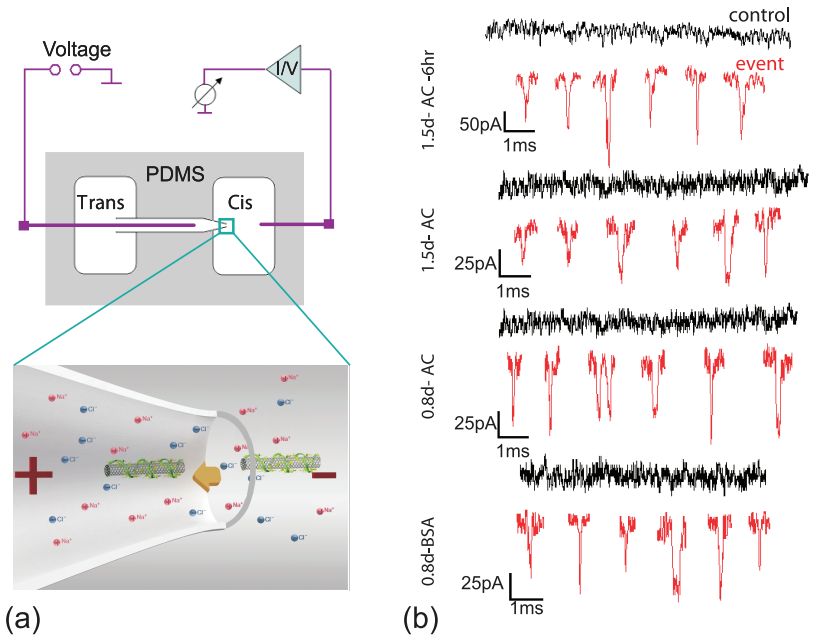

Figure 3. (a) Sample cell, nanocapillary, and measuring circuits, with an illustration of the translocation process. (b) Typical current traces of biomolecule−SWNT hybrids.

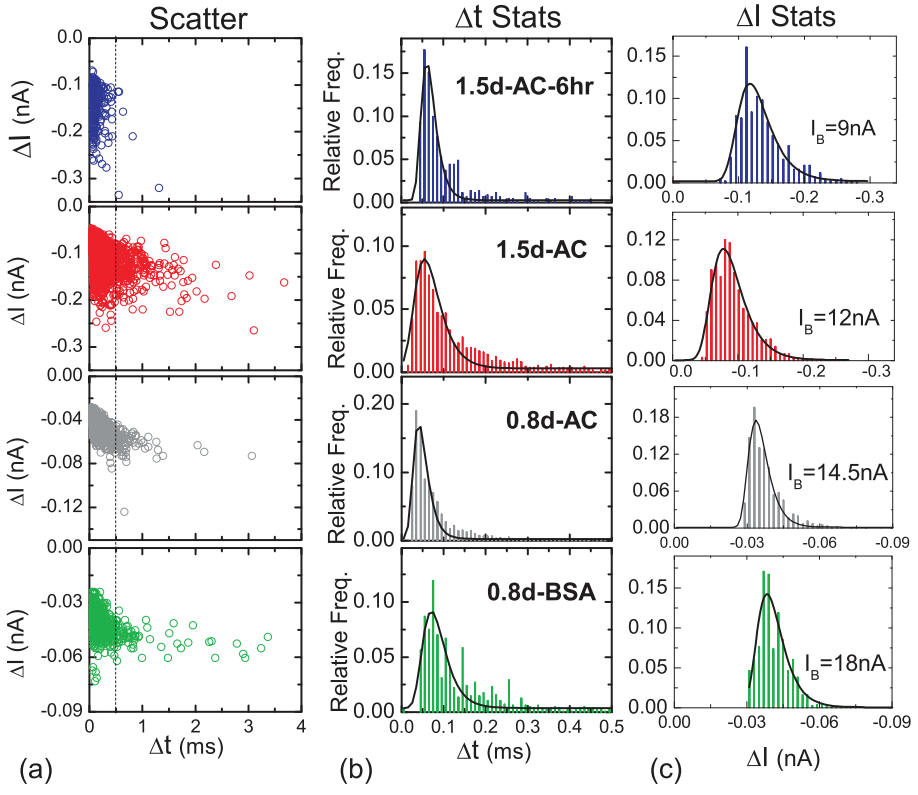

Figure 4. (a) Scatter plot of event duration and peak current for the different SWNT−biomolecule hybrids, with a 0.1 mg/mL concentration in buffered 0.5 M NaCl solution at pH 8, and +300 mV potential. (b,c) Duration and peak event current for the hybrids.

region to be rare and focus on analyzing the statistics of $\Delta t \leq 0.5$ ms. We note that the apparent shape of the scatter plot can vary between samples for the same hybrid due to the deviation in dispersion quality (*i.e.*, the fraction of isolated SWNT hybrids can vary between different tests). By separately analyzing the Δt and ΔI, we aim to establish the correlation between the measured event signals and the physical characteristics of the biomolecule−SWNT hybrids.

First, Figure 5a summarizes the measured Δt for the different hybrids, with each data point being an average of five separate tests. The 1.5d-AC hybrid shows a

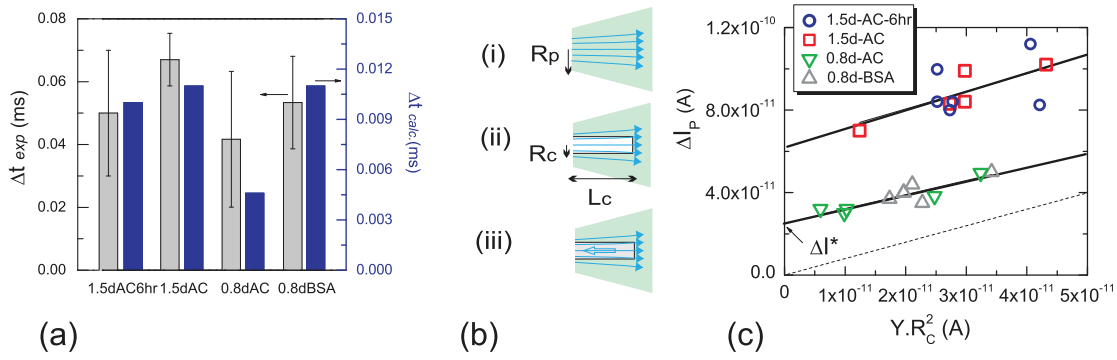

Figure 5. (a) Mean Δt from nanocapillary experiments (left axis) and from Zetasizer measurements (right axis). (b) Schemes illustrating how the current level may change from (i) steady state I_B; to (ii) when an insulating rod is present blocking the flow of charges with its occupied volume; to (iii) when the rod is replaced with a conducting one, not only inducing ionic current exclusion but also giving a counteracting electric field. (c) ΔI_p as a function of YR_c^2 for different runs of experiments for all hybrids. Extrapolating the best-fit line for group-1.5d and group-0.8d yields a *y*-intercept ΔI^*, which we suggest to relate to the SWNT core polarizability. The dashed line shows the trend with a gradient of 1 and zero intercept.

modal translocation duration of 65 μs, in agreement with ref 32 for the same SWNT and biomolecule combination. Altering the SWNT length and/or coating shifts the modal Δt. As a hybrid is being driven through the pore, we postulate it to align along the central axis of the channel to allow efficient passage of the hybrid. Hence, the total dwell time in the concentrated electric field region is directly related to the hybrids' length. Comparing the results from 1.5d-AC and 1.5d-AC-6hr (*i.e.*, the two hybrids that should share similar molecular characteristics except for their lengths), a difference is observed between their translocation times. The ratio between the average Δt of 1.5d-AC and 1.5d-AC-6hr is 0.067:0.05≈1.34, in agreement with the ratio between the AFM measured lengths (*i.e.*, $L_{1.5d-AC}$:$L_{1.5d-AC-6hr}$ = 147:115≈1.28). However, this rule does not apply for all samples, such that the overall ranking of Δt for the four hybrids is different from the ranking of the physical lengths of the dried hybrids as determined by AFM. We will postulate the reasons for the observed discrepancy in the Discussion section.

Event Current ΔI. Next we analyze the result of ΔI dependence on the hybrids' properties. The histograms of ΔI based on the scatter plots from each hybrid are shown in Figure 4c. Due to the difference in pore diameter (as represented by the corresponding baseline I_B), the modal values of event current vary between different runs, even for the same hybrid. In our experiment, ΔI is measured as the peak change in event current observed during translocation. Based on the consideration of ionic blockage, ΔI is expected to occur when the whole hybrid has just fully entered, such that the blockage of charges is most significant in the field focusing region. Since the hybrids' length is much greater than the pore diameter, and the high intensity electrical field lines are concentric to the capillary axis, they have a high probability to enter with their longitudinal axis aligned with the capillary axis. Figure 5b(i,ii) illustrate such a configuration.

In order to extract meaningful information from the ΔI statistics, we model ΔI by considering the charge exclusion effect by only considering the physical occupancy of the hybrid, assumed to be rod-shaped. Treating the capillary tip as a cone (having a fixed cone angle $\tan\theta = 0.15$) with pore radius R_p, containing a salt solution of conductivity 5 S/m, we can derive how ΔI changes with respect to parameters, such as the radius (R_c) and the length (L_c) of the hybrid. We approximate $\Delta I \sim Y_o(R_p)R_c^2$, where $Y_o = K_o R_p^{-1.08}$ A/m^2 is a geometry-dependent factor affected by R_c, the size of the nanopore; $K_o \sim 0.108$ A/m$^{0.92}$ is the constant prefactor determined by the solution conductivity and the conical shape of the pore.

Since $I_B \sim 0.15\pi g(d_b/l)R_p \sim 0.77R_p$ (see Methods for the dependence of I_B on R_p), we obtain

$$\Delta I \sim Y(I_B)R_c^2 \qquad (1)$$

where $Y \sim 0.082 I_B^{-1.08}$ A/m^2. To test this relation, we plot the experimental ΔI_p (the modal ΔI) against YR_c^2, where R_c is taken as the radius of the hybrids measured by AFM. Several runs for each hybrid are plotted together in Figure 5c. The data are located in two distinct regions: 1.5d-AC and 1.5d-AC-6hr lie in the upper region (Group-1.5d); 0.8d-AC and 0.8d-BSA lie in the lower region (Group-0.8d). By a linear fit over the two regions, the gradients D (dimensionless) are found to be $D \sim 0.9$ and $D \sim 0.7$ for Group-1.5d and Group-0.8d, respectively. The slopes agree reasonably with the predicted value $D = 1$ according to eq 1.

The above analysis predicts that, with $R_c \to 0$, it follows that $\Delta I \to 0$. However, for the two groups of data, extrapolating the fit to $R_c = 0$ yields an offset ΔI^*. The values of ΔI^* are different: $\Delta I^* = 5.1 \times 10^{-11}$ A for Group-1.5d and 2.5×10^{-11} A for Group-0.8d. The offset should have weak, or no R_c dependence, because (1) the model in eq 1 already takes into account all geometry effects; (2) for Group-0.8d, the 0.8d-BSA hybrids have a mean $R_c = 0.95$ nm, and the 0.8d-AC hybrids have a mean $R_c = 0.65$ nm. However, they both lie on the line having the same offset. On the basis of these observations, we modify eq 1 as

$$\Delta I \sim Y(I_B)R_c^2 + \Delta I^* \qquad (2)$$

It is the presence of ΔI^* which separates the two hybrid groups in the plot of ΔI_p against YR_c^2 in Figure 5c. We will further discuss the significance of this offset ΔI^* in the Discussion section.

DISCUSSION

As shown by the Results section, the event dwell time Δt and event current ΔI combination is specific to a particular SWNT hybrid. However, the correlation is not straightforward and requires further elaboration.

First, Δt is clearly a function of other factors in addition to the length of the hybrids. Since the hybrids are present in a solution, it may be that the hydrodynamic interaction or unspecific binding manifests a more dominating effect than the lengths of the hybrids when concerning the values of Δt. An alternative explanation accounting for the ranking observed in Figure 5a can be given by considering the hydrodynamic size R_z and the mobilities $M_{complex}$ of the hybrids in solution (shown in Table 1). Taking a simple picture of a hybrid moving under an applied electric field E, the drift velocity V_{drift} is determined by $V_{drift} = M_{complex}E$. Thus, the time for each hybrid to travel through a distance R_z is $T_R = R_z/(M_{complex}E)$. Using the R_z and $M_{complex}$ values determined by our Zetasizer measurements (shown in Table 1), we find the ranking of $R_z/(ME)$ to resemble that of the Δt measured by resistive pulse sensing with the nanocapillaries. Moreover, taking $E = 10^6$ V/m (*i.e.*, an electric field similar to that used in our experiments), we find $T_R \sim 5-10\ \mu$s, which presents a lower limit for Δt. This is because $M_{complex}$ is measured as the free-hybrid mobility; confinement imposed by the nanopore and the possible polarization of the charged DNA[87] would result in greater hindrance, thus lowering the translocation speed.[34] On the other hand, Δt has similar magnitude to T_R. For translocation of flexible or semiflexible long chain molecules studied in nanopores with diameters above 10 nm,[88] Δt is dependent on the rate of uncoiling of polymer chains.[88] The rigid structure of the hybrid means that once the hybrid has the correct orientation to enter, it traverses the pore channel readily with small hindrance. We thus suggest that Δt for a rigid SWNT–biomolecule hybrid reflects the ratio between hydrated molecular size and mobility, where $M_{complex}$ includes factors due to the zeta-potential and the shape-dependent drag coefficient of the molecule.

For the analysis of the event current, the origin of the detected offset current, ΔI^* in eq 2, also requires further discussion. One possible explanation for ΔI^* comes from the intrinsic conduction characteristics of the SWNTs. As a conducting element is placed inside a uniform electric field, an opposing electric field is generated within the element, which reduces or even cancels out the overall field effects in the vicinity due to induced polarization.[89] This effect is schematically illustrated in Figure 5b(iii). Such an electric field shielding may introduce a further component which reduces the current level; that is, it increases the apparent current blockage ΔI. The large diameter 1.5d SWNT cores are of either semiconducting with a small band gap or of metallic characteristics; this is because the fundamental band gap, associated with the eh_{11} transition is inversely proportional to the radius of a SWNT (*i.e.*, $E_g \sim 1/R$)[48,75] and the fact that we did not observe emission in PLE for $\lambda_{em} < 1600$ nm. All the above results indicate the *isolated* s-SWNTs present in the P2 hybrids have $E_g < 0.77$ eV. On the other hand, the 0.8d SWNTs are enriched with (6,5) ($E_g \sim 2.15$ eV) and other chiralities with $E_g > 1$ eV (see results of Raman and photoluminescence spectroscopies). Finally, computational simulation by ref 90 has shown that the polarizability of SWNTs is proportional to the square of their radius. All of the above analysis seems to support that the temporary polarization of the SWNT core may contribute to a value ΔI^* larger for Group-1.5d than for Group-0.8d.

Another key feature of eq 2 is the gradient for each data group, where ΔI is plotted against $Y(I_B)R_c^2$. Agreement between the experimental and predicted gradients indicates that the net blockage current $\Delta I - \Delta I^*$ is proportional to the cross-sectional area of the hybrid (*i.e.*, $\Delta I - \Delta I^* \propto R_c^2$). The net blockage current results from the entry of a single molecular hybrid into a pore. Since the experimental gradients are between 0.9 and 0.7 compared to the theoretical gradient of 1, the estimation for the radius will have a deviation of $(0.9/1)^{1/2}$ or $(0.7/1)^{1/2}$, according to eq 2. This yields a ~15% error for $R_c \sim 1$ nm. Therefore, eq 2 can be seen as a form of "calibration curve". Once the correlation between ΔI and R_c^2 is established, rod-like hybrids of other sizes can be directly measured even for nanocapillaries of different pore sizes. In other words, using a fixed SWNT core, provided the interaction between the SWNTs and the molecules is sufficiently strong, we may use SWNTs as carriers to detect short DNA oligomer or polypeptides.

In summary, spectroscopic measurements reveal doping of the SWNTs by the surface-bound biomolecules. The strong interaction associated with SWNT and DNA or protein molecules underpins the feasibility of translocating stable hybrids through a nanocapillary for resistive pulse sensing. The signals resulting from a nanocapillary detection can then be used to characterize the structure of hybrids. The event dwell time reveals the ratio between hydrodynamic size and mobility. For the event current, the rigid structure of the hybrids also allowed us to correlate the peak event current to the predicted current change induced by the ionic blockage of a rod. We detect an additional offset in the event current, assigned to the induced polarization of the SWNT core. We can thus estimate the cross-sectional thickness of SWNT–biomolecule hybrids, even for measurements in nanocapillaries of different

sizes. This could allow one to compare the resistive pulse results from different experiments and determine the nature of the biomolecular binding layer by adapting a standard SWNT "carrier". Thus, small DNA oligomers and polypeptides might be directly analyzed in a large conventional unmodified solid-state nanopore, paving the way to the understanding of generic inorganic–organic hybrid transport through nanopores and allowing for analysis of a wide range of molecules that can be bound with SWNTs.

METHODS

Preparation of SWNT–Biomolecule Hybrids. For carbon nanotubes, CoMoCAT (6,5)-enriched SWNTs and P2 arc-discharged SWNTs were purchased from Sigma-Aldrich and Carbon Solutions, respectively. $(AC)_{15}$ oligomers (Invitrogen) and BSA protein (Sigma-Aldrich) were wrapped around SWNTs through the following steps which involve a two-stage sonication. First, a 1 mg/mL SWNT in 0.1 M sodium chloride (NaCl) solution (Trisethylenediaminetetraacetic acid, or Tris-EDTA buffer, pH 8) was prepared by tip sonication for 2 h (or 6 h) as for refs 13 and 56. Subsequently, this dispersion was mixed with the biomolecule dispersion (1 mg/mL biomolecule in 0.1 M NaCl, Tris-EDTA buffer, pH 8) at a 1:1 volume ratio, resulting in a final concentration of SWNTs in BSA solution of 0.5 mg/mL. For $(AC)_{15}$ wrapping, the mixture was left to incubate for 48 h, followed by sonication in an ice-cooled bath for an additional 2 h. The BSA was found to achieve optimal coating without incubation (determined by comparing the absorption spectrum of the dispersion after incubation for different times). After sonication, the SWNT–biomolecule hybrids were subjected to centrifugation (15 000*g*, 30 min) to remove both unstable SWNTs and hybrids.[38]

Atomic Force Microscopy. The diameter of pristine SWNTs was investigated by AFM studies. The pristine SWNTs were prepared as follows: 0.5 mg of starting material (CoMoCAT (6,5)-enriched SWNTs and P2 arc-discharged SWNTs, respectively) was dispersed in 30 mL of *N*-methyl-2-pyrrolidone (NMP) at 15 °C in a 180 W horn sonicator (Branson sonifier, S-450A) for 2 h. The dispersions were then ultracentrifuged using a TH-641 swinging bucket rotor in a Sorvall WX-100 ultracentrifuge at 40000 rpm for another 2 h. For each material, a 1:100 dilution in NMP was drop-casted on clean standard Si/SiO_2 substrates and then dried first at room temperature for 12 h and finally in oven at 70 °C for 3 h.

AFM of SWNT–biomolecule hybrids was prepared as follows. The centrifuged conjugate solutions (see procedures above) were filtered through a 100 kDa filter (Amicon Ultra Millipore) under 14 000*g* for 7 min to remove the free $(AC)_{15}$ or BSA in solution. The remaining concentrated filtrate was redispersed and deposited onto cleaved mica surface (0.5 M $MgCl_2$ treated). All the atomic force microscopic images were obtained under the tapping mode. The obtained images were then analyzed with Gwyddion.

Raman Spectroscopy. As-received SWNT powders were deposited on a SiO_2/Si substrate. The hybrids were also drop-cast on 300 nm SiO_2/Si substrates and left to evaporate at room temperatures. Raman spectra were acquired at 514.5 and 632.8 nm using a Renishaw InVia micro-Raman spectrometer. The power on the samples was kept <1 mW in order to avoid possible heating effects. We used Renishaw Holographic Notch Filters having ~50 cm^{-1} cut off frequency at 514.5 and 632.8 nm.

Photoluminescence. PLE of the dispersions was carried out using a Horiba Jobin-Yvon excitation–emission spectrofluorometer (Fluorolog 3). We used a 14.7 nm slit for the double grating excitation monochromator and 60 nm for the single grating emission monocromator blazed at 1200 nm. The scan step was 5 nm for 400–680 nm excitation, covering the eh_{22} range of our nanotubes.[75,76] The PL data were corrected by background subtraction and normalized according to the lamp intensity profile using the same excitation slit. The optical absorbance of the SWNT–biomolecule hybrid samples in water was adjusted by dilution using water to ~0.1–0.2 to avoid reabsorption effects.

Translocation Experiment. All nanocapillaries were produced by Pipette Puller P-2000 using quartz glass with an outer diameter of 0.5 mm and a wall thickness of 0.1 mm. Pulling parameters were optimized to obtain nanopore openings between 13 and 60 nm. The capillary–PDMS fluid cell was constructed as shown in Figure 3a. Electrical potentials were delivered by Ag/AgCl electrodes placed separately at the *cis*- and *trans*-chamber. The fully constructed cell was then cleaned using oxygen plasma and then filled with salt solution using a desiccator.

For all ionic current measurements, we used an Axopatch 200B (Axon Instruments, USA) amplifier in voltage-clamp mode with the internal four-pole Bessel filter at 10 kHz bandwidth. Real-time current/voltage traces were recorded using PClamp10.0. These current–time traces were then analyzed in Clampfit to determine the event current and event dwell time. For blank salt solutions, Figure SI1a shows a slightly asymmetrical $I-V$ curve characteristic to the conical pore configuration.

The inner diameter, d_i, of the nanopore can be estimated through a simplified equation for conical nanocapillaries:[30] $d_i = 4G_{cap}l/\pi g d_b$. Here, l is the length (in unit of meters) of the conical part, d_b the diameter (in meters) of the capillary before starting to converge, g the specific conductance (in S/m) of the salt solution, and G_{cap} the nanocapillary conductance (in S). In our case, l = 0.001 m and $d_b = 3 \times 10^{-4}$ m. Measurements were performed in 0.5 M NaCl salt solutions (Tris-EDTA buffer, pH 8), thus g = 5 S/m (measured by Mettler Toledo pH/ion meter SevenMulti S80). G_{cap} is the ratio between the open pore baseline current (I_B) to the voltage (300 mV), that is, $G_{cap} = I_B/0.3$ S. The translocation events were detectable when $I_B \sim 5-24$ nA, equivalent to pore diameters in the 13–60 nm range. For translocation experiments, the number of events in each run ranged between 400 and 3000.

Conflict of Interest: The authors declare no competing financial interest.

Acknowledgment. The authors thank A. Hall for helpful advice, and H. Beeson for characterization work. Y.Y.S.H. thanks financial support from the Oppenheimer Fellowship and a Homerton College Fellowship. T.H. acknowledges support from the Royal Academy of Engineering, Churchill College, Cambridge and National Natural Science Foundation of China (Grant No. 61150110487). F.B. acknowledges funding from the Newton Trust and the Newton International Fellowship. A.C.F. acknowledges the ERC Grant NANOPOTS, a Royal Society Wolfson Research Merit Award, EPSRC Grants EP/K01711X/1, EP/K017144/1, and EP/G042357/1. U.F.K. acknowledges funding by the Emmy Noether Program of the Deutsche Forshungsgesellschaft. This work is supported by The National Basic Research Program of China (2011CB707605) and National Natural Science Foundation of China (51005048).

Supporting Information Available: Nanocapillary *IV* and real-time event traces of nanocapillary; translocation characteristics associated with hybrid bundling. This material is available free of charge *via* the Internet at http://pubs.acs.org.

REFERENCES AND NOTES

1. Dang, X.; Yi, H.; Ham, M. H.; Qi, J.; Yun, D. S.; Ladewski, R.; Strano, M. S.; Hammond, P. T.; Belcher, A. M. Virus-Templated Self-Assembled Single-Walled Carbon Nanotubes for Highly Efficient Electron Collection in Photovoltaic Devices. *Nat. Nanotechnol.* **2011**, *6*, 377–384.
2. Shi, Y.; Hasan, T.; Babu, N. H.; Torrisi, F.; Milana, S.; Ferrari, A. C.; Cardwell, D. A. Synthesis of $YBa_2Cu_3O_{7-d}$ and Y_2BaCuO_5 Nanocrystalline Powders for YBCO Superconductors Using Carbon Nanotube Templates. *ACS Nano* **2012**, *6*, 5395–5403.

3. Keren, K.; Berman, R. S.; Buchstab, E.; Sivan, U.; Braun, E. DNA-Templated Carbon Nanotube Field-Effect Transistor. *Science* **2003**, *302*, 1380–1382.
4. Wei, A.; Sun, X. W.; Wang, J. X.; Lei, Y.; Cai, X. P.; Li, C. M.; Dong, Z. L.; Huang, W. Enzymatic Glucose Biosensor Based on ZnO Nanorod Array Grown by Hydrothermal Decomposition. *Appl. Phys. Lett.* **2006**, *89*, 123902-3.
5. Yi, H.; Ghosh, D.; Ham, M.-H.; Qi, J.; Barone, P. W.; Strano, M. S.; Belcher, A. M. M13 Phage-Functionalized Single-Walled Carbon Nanotubes as Nanoprobes for Second Near-Infrared Window Fluorescence Imaging of Targeted Tumors. *Nano Lett.* **2012**, *12*, 1176–1183.
6. Heller, D. A.; Jin, H.; Martinez, B. M.; Patel, D.; Miller, B. M.; Yeung, T.-K.; Jena, P. V.; Hobartner, C.; Ha, T.; Silverman, S. K.; *et al.* Multimodal Optical Sensing and Analyte Specificity Using Single-Walled Carbon Nanotubes. *Nat. Nanotechnol.* **2009**, *4*, 114–120.
7. Aili, D.; Gryko, P.; Sepulveda, B.; Dick, J. A. G.; Kirby, N.; Heenan, R.; Baltzer, L.; Liedberg, B.; Ryan, M. P.; Stevens, M. M. Polypeptide Folding-Mediated Tuning of the Optical and Structural Properties of Gold Nanoparticle Assemblies. *Nano Lett.* **2011**, *11*, 5564–5573.
8. Huang, Y. Y. S.; Terentjev, E. M.; Oppenheim, T.; Lacour, S. P.; Welland, M. E. Fabrication and Electromechanical Characterization of Near-Field Electrospun Composite Fibers. *Nanotechnology* **2012**, *23*, 105305.
9. Bertulli, C.; Beeson, H.; Hasan, T.; Huang, Y. Y. S. Spectroscopic Characterization of Protein-Wrapped Single-Wall Carbon Nanotubes and Quantification of Their Cellular Uptake in Multiple Cell Generations. *Nanotechnology* **2013**, *24*, 265102.
10. Liu, Z.; Tabakman, S. M.; Chen, Z.; Dai, H. Preparation of Carbon Nanotube Bioconjugates for Biomedical Applications. *Nat. Protoc.* **2009**, *4*, 1372–1381.
11. Grigoryan, G.; Kim, Y. H.; Acharya, R.; Axelrod, K.; Jain, R. M.; Willis, L.; Drndic, M.; Kikkawa, J. M.; DeGrado, W. F. Computational Design of Virus-like Protein Assemblies on Carbon Nanotube Surfaces. *Science* **2011**, *332*, 1071–1076.
12. Boghossian, A. A.; Zhang, J.; Barone, P. W.; Reuel, N. F.; Kim, J.-H.; Heller, D. A.; Ahn, J. H.; Hilmer, A. J.; Rwei, A.; Arkalgud, J. R.; *et al.* Near-Infrared Fluorescent Sensors Based on Single-Walled Carbon Nanotubes for Life Sciences Applications. *ChemSusChem* **2011**, *4*, 848–863.
13. Zheng, M.; Jagota, A.; Strano, M. S.; Santos, A. P.; Barone, P.; Chou, S. G.; Diner, B. A.; Dresselhaus, M. S.; Mclean, R. S.; Onoa, G. B.; *et al.* Structure-Based Carbon Nanotube Sorting by Sequence-Dependent DNA Assembly. *Science* **2003**, *302*, 1545–1548.
14. Kam, N. W. S.; O'Connell, M.; Wisdom, J. A.; Dai, H. Carbon Nanotubes as Multifunctional Biological Transporters and Near-Infrared Agents for Selective Cancer Cell Destruction. *Proc. Natl. Acad. Sci. U.S.A.* **2005**, *102*, 11600–11605.
15. Karajanagi, S. S.; Vertegel, A. A.; Kane, R. S.; Dordick, J. S. Structure and Function of Enzymes Adsorbed onto Single-Walled Carbon Nanotubes. *Langmuir* **2004**, *20*, 11594–11599.
16. Gigliotti, B.; Sakizzie, B.; Bethune, D. S.; Shelby, R. M.; Cha, J. N. Sequence-Independend Helical Wrapping of Single-Walled Carbon Nanotubes by Long Genomic DNA. *Nano Lett.* **2006**, *6*, 159–164.
17. Zhao, X.; Johnson, J. K. Simulation of Adsorption of DNA on Carbon Nanotubes. *J. Am. Chem. Soc.* **2007**, *129*, 10438–10445.
18. Balamurugan, K.; Gopalakrishnan, R.; Raman, S. S.; Subramanian, V. Exploring the Changes in the Structure of α-Helical Peptides Adsorbed onto a Single Walled Carbon Nanotube Using Classical Molecular Dynamics Simulation. *J. Phys. Chem. B* **2010**, *114*, 14048–14058.
19. Cathcart, H.; Nicolosi, V.; Hughes, J. M.; Blau, W. J.; Kelly, J. M.; Quinn, S. J.; Coleman, J. N. Ordered DNA Wrapping Switches on Luminescence in Single-Walled Nanotube Dispersions. *J. Am. Chem. Soc.* **2008**, *130*, 12734–12744.
20. Campbell, J. F.; Tessmer, I.; Thorp, H. H.; Erie, D. A. Atomic Force Microscopy Studies of DNA-Wrapped Carbon Nanotube Structure and Binding to Quantum Dots. *J. Am. Chem. Soc.* **2008**, *130*, 10648–10655.
21. Lamprecht, C.; Danzberger, J.; Lukanov, P.; Tilmaciu, C. M.; Galibert, A. M.; Soula, B.; Flahaut, E.; Gruber, H. J.; Hinterdorfer, P.; Ebner, A.; *et al.* AFM Imaging of Functionalized Double-Walled Carbon Nanotubes. *Ultramicroscopy* **2009**, *109*, 899–906.
22. Helmholtz, H. V. Ueber einige Gesetze der Vertheilung elektrischer Ströme in körperlichen Leitern, mit Anwendung auf die thierisch-elektrischen Versuche (Anfang). *Ann. Phys. Chem.* **1853**, *89*, 211–233.
23. Huang, Y. Y.; Terentjev, E. M. Transparent Electrode with a Nanostructured Coating. *ACS Nano* **2011**, *5*, 2082–2089.
24. Dekker, C. Solid-State Nanopores. *Nat. Nanotechnol.* **2007**, *2*, 209–215.
25. Venkatesan, B. M.; Bashir, R. Nanopore Sensors for Nucleic Acid Analysis. *Nat. Nanotechnol.* **2011**, *6*, 615–624.
26. Schneider, G. G. F.; Kowalczyk, S. W.; Calado, V. E.; Pandraud, G.; Zandbergen, H. W.; Vandersypen, L. M. K.; Dekker, C. DNA Translocation through Graphene Nanopores. *Nano Lett.* **2010**, *10*, 3163–3167.
27. Wanunu, M. Nanopores: A Journey towards DNA Sequencing. *Phys. Life Rev.* **2012**, *9*, 125–158.
28. Li, J.; Gershow, M.; Stein, D.; Brandin, E.; Golovchenko, J. A. DNA Molecules and Configurations in a Solid-State Nanopore Microscope. *Nat. Mater.* **2003**, *2*, 611–615.
29. Keyser, U. F. Controlling Molecular Transport through Nanopores. *J. R. Soc. Interface* **2011**, *8*, 1369–1378.
30. Storm, A. J.; Chen, J. H.; Zandbergen, H. W.; Dekker, C. Translocation of Double-Strand DNA through a Silicon Oxide Nanopore. *Phys. Rev. E* **2005**, *71*, 051903.
31. Howorka, S.; Siwy, Z. Nanopore Analytics: Sensing of Single Molecules. *Chem. Soc. Rev.* **2009**, *38*, 2360–2384.
32. Hall, A. R.; Keegstra, J. M.; Duch, M. C.; Hersam, M. C.; Dekker, C. Translocation of Single-Wall Carbon Nanotubes through Solid-State Nanopores. *Nano Lett.* **2011**, *11*, 2446–2450.
33. Steinbock, L. J.; Otto, O.; Chimerel, C.; Gornall, J.; Keyser, U. F. Detecting DNA Folding with Nanocapillaries. *Nano Lett.* **2010**, *10*, 2493–2497.
34. Keyser, U. F.; van Dorp, S.; Lemay, S. G. Tether Forces in DNA Electrophoresis. *Chem. Soc. Rev.* **2010**, *39*, 939–947.
35. Wanunu, M.; Dadosh, T.; Ray, V.; Jin, J.; McReynolds, L.; Drndic, M. Rapid Electronic Detection of Probe-Specific MicroRNAs Using Thin Nanopore Sensors. *Nat. Nanotechnol.* **2010**, *5*, 807–814.
36. Hirayama, K.; Akashi, S.; Furuya, M.; Fukuhara, K. Rapid Confirmation and Revision of the Primary Structure of Bovine Serum Albumin by ESIMS and Frit-FAB LC/MS. *Biochem. Biophys. Res. Commun.* **1990**, *173*, 639–646.
37. Bendedouch, D.; Chen, S. H. Structure and Interparticle Interactions of Bovine Serum Albumin in Solution Studied by Small-Angle Neutron Scattering. *J. Phys. Chem.* **1983**, *87*, 1473–1477.
38. Holt, B. D.; Dahl, K. N.; Islam, M. F. Quantification of Uptake and Localization of Bovine Serum Albumin-Stabilized Single-Wall Carbon Nanotubes in Different Human Cell Types. *Small* **2011**, *7*, 2348–2355.
39. Hu, P.; Zhang, C.; Fasoli, A.; Scardaci, V.; Pisana, S.; Hasan, T.; Robertson, J.; Milne, W. I.; Ferrari, A. C. Hysteresis Suppression in Self-Assembled Single-Wall Nanotube Field Effect Transistors. *Physica E* **2008**, *40*, 2278–2282.
40. Hu, P.; Fasoli, A.; Park, J.; Choi, Y.; Estrela, P.; Maeng, S. L.; Milne, W. I.; Ferrari, A. C. Self-Assembled Nanotube Field-Effect Transistors for Label-Free Protein Biosensors. *J. Appl. Phys.* **2008**, *104*, 074310-5.
41. Ferrari, A. C.; Robertson, J. Raman Spectroscopy of Amorphous, Nanostructured, Diamond-like Carbon, and Nanodiamond. *Philos. Trans. R. Soc. A* **2004**, *362*, 2477.
42. Ferrari, A. C.; Basko, D. M. Raman Spectroscopy as a Versatile Tool for Studying the Properties of Graphene. *Nat. Nanotechnol.* **2013**, *8*, 253.
43. Rao, A. M.; Richter, E.; Bandow, S.; Chase, B.; Eklund, P. C.; Williams, K. A.; Fang, S.; Subbaswamy, K. R.; Menon, M.; Thess, A.; *et al.* Diameter-Selective Raman Scattering from Vibrational Modes in Carbon Nanotubes. *Science* **1997**, *275*, 187–191.

44. Telg, H.; Maultzsch, J.; Reich, S.; Hennrich, F.; Thomsen, C. Chirality Distribution and Transition Energies of Carbon Nanotubes. *Phys. Rev. Lett.* **2004**, *93*, 177401.
45. Meyer, J. C.; Paillet, M.; Michel, T.; Moreac, A.; Neumann, A.; Duesberg, G. S.; Roth, S.; Sauvajol, J. L. Raman-Modes of Index-Identified Free-Standing Single-Walled Carbon Nanotubes. *Phys. Rev. Lett.* **2005**, *95*, 217401.
46. Fantini, C.; Jorio, A.; Souza, M.; Strano, M. S.; Dresselhaus, M. S.; Pimenta, M. A. Optical Transition Energies for Carbon Nanotubes from Resonant Raman Spectroscopy: Environment and Temperature Effects. *Phys. Rev. Lett.* **2004**, *93*, 147406.
47. Araujo, P. T.; Doorn, S. K.; Kilina, S.; Tretiak, S.; Einarsson, E.; Maruyama, S.; Chacham, H.; Pimenta, M. A.; Jorio, A. Third and Fourth Optical Transitions in Semiconducting Carbon Nanotubes. *Phys. Rev. Lett.* **2007**, *98*, 067401.
48. Kataura, H.; Kumazawa, Y.; Maniwa, Y.; Umezu, I.; Suzuki, S.; Ohtsuka, Y.; Achiba, Y. Optical Properties of Single-Wall Carbon Nanotubes. *Synth. Met.* **1999**, *103*, 2555–2558.
49. Piscanec, S.; Lazzeri, M.; Robertson, J.; Ferrari, A. C.; Mauri, F. Optical Phonons in Carbon Nanotubes: Kohn Anomalies, Peierls Distortions, and Dynamic Effects. *Phys. Rev. B* **2007**, *75*, 035427.
50. Jorio, A.; Souza, A. G.; Dresselhaus, G.; Dresselhaus, M. S.; Swan, A. K.; Unlu, M. S.; Goldberg, B. B.; Pimenta, M. A.; Hafner, J. H.; Lieber, C. M.; *et al.* G-Band Resonant Raman Study of 62 Isolated Single-Wall Carbon Nanotubes. *Phys. Rev. B* **2002**, *65*, 155412.
51. Lazzeri, M.; Piscanec, S.; Mauri, F.; Ferrari, A. C.; Robertson, J. Phonon Linewidths and Electron−Phonon Coupling in Graphite and Nanotubes. *Phys. Rev. B* **2006**, *73*, 155426.
52. Das, A.; Sood, A. K.; Govindaraj, A.; Saitta, A. M.; Lazzeri, M.; Mauri, F.; Rao, C. N. R. Doping in Carbon Nanotubes Probed by Raman and Transport Measurements. *Phys. Rev. Lett.* **2007**, *99*, 136803.
53. Tsang, J. C.; Freitag, M.; Perebeinos, V.; Liu, J.; Avouris, P. Doping and Phonon Renormalization in Carbon Nanotubes. *Nat. Nanotechnol.* **2007**, *2*, 725–730.
54. Ferrari, A. C.; Robertson, J. Interpretation of Raman Spectra of Disordered and Amorphous Carbon. *Phys. Rev. B* **2000**, *61*, 14095.
55. Ferrari, A. C. Raman Spectroscopy of Graphene and Graphite: Disorder, Electron−Phonon Coupling, Doping and Nonadiabatic Effects. *Solid State Commun.* **2007**, *143*, 47–57.
56. Huang, Y. Y.; Knowles, T. W.; Terentjev, E. M. Strength of Nanotubes, Filaments, and Nanowires from Sonication-Induced Scission. *Adv. Mater.* **2009**, *21*, 3945–3948.
57. Huang, Y. Y.; Terentjev, E. M. Dispersion of Carbon Nanotubes: Mixing, Sonication, Stabilization, and Composite Propertie. *Polymers* **2012**, *4*, 275–295.
58. Piscanec, S.; Lazzeri, M.; Mauri, F.; Ferrari, A. C.; Robertson, J. Kohn Anomalies and Electron−Phonon Interactions in Graphite. *Phys. Rev. Lett.* **2004**, *93*, 185503.
59. Bonaccorso, F.; Hasan, T.; Tan, P. H.; Sciascia, C.; Privitera, G.; Di Marco, G.; Gucciardi, P. G.; Ferrari, A. C. Density Gradient Ultracentrifugation of Nanotubes: Interplay of Bundling and Surfactants Encapsulation. *J. Phys. Chem. C* **2010**, *114*, 17267–17285.
60. Bachilo, S. M.; Strano, M. S.; Kittrell, C.; Hauge, R. H.; Smalley, R. E.; Weisman, R. B. Structure-Assigned Optical Spectra of Single-Walled Carbon Nanotubes. *Science* **2002**, *298*, 2361–2366.
61. Tan, P. H.; Rozhin, A. G.; Hasan, T.; Hu, P.; Scardaci, V.; Milne, W. I.; Ferrari, A. C. Photoluminescence Spectroscopy of Carbon Nanotube Bundles: Evidence for Exciton Energy Transfer. *Phys. Rev. Lett.* **2007**, *99*, 137402.
62. Tan, P. H.; Hasan, T.; Bonaccorso, F.; Scardaci, V.; Rozhin, A. G.; Milne, W. I.; Ferrari, A. C. The Shear Mode of Multilayer Graphene. *Physica E* **2008**, *40*, 2352–2359.
63. Hasan, T.; Scardaci, V.; Tan, P. H.; Rozhin, A. G.; Milne, W. I.; Ferrari, A. C. Stabilization and "Debundling" of Single-Wall Carbon Nanotube Dispersions in *N*-Methyl-2-pyrrolidone (NMP) by Polyvinylpyrrolidone (PVP). *J. Phys. Chem. C* **2007**, *111*, 12594–12602.
64. Hasan, T.; Tan, P. H.; Bonaccorso, F.; Rozhin, A.; Scardaci, V.; Milne, W.; Ferrari, A. C. Polymer-Assisted Isolation of Single Wall Carbon Nanotubes in Organic Solvents for Optical-Quality Nanotube-Polymer Composites. *J. Phys. Chem. C* **2008**, *112*, 20227–20232.
65. McDonald, T. J.; Blackburn, J. L.; Metzger, W. K.; Rumbles, G.; Heben, M. J. Chiral-Selective Protection of Single-Walled Carbon Nanotube Photoluminescence by Surfactant Selection. *J. Phys. Chem. C* **2007**, *111*, 17894–17900.
66. Niyogi, S.; Boukhalfa, S.; Chikkannanavar, S. B.; McDonald, T. J.; Heben, M. J.; Doorn, S. K. Selective Aggregation of Single-Walled Carbon Nanotubes *via* Salt Addition. *J. Am. Chem. Soc.* **2007**, *129*, 1898.
67. Perebeinos, V.; Tersoff, J.; Avouris, P. Effect of Exciton−Phonon Coupling in the Calculated Optical Absorption of Carbon Nanotubes. *Phys. Rev. Lett.* **2005**, *94*, 027402.
68. Plentz, F.; Ribeiro, H. B.; Jorio, A.; Strano, M. S.; Pimenta, M. A. Direct Experimental Evidence of Exciton−Phonon Bound States in Carbon Nanotubes. *Phys. Rev. Lett.* **2005**, *95*, 247401.
69. Lefebvre, J.; Finnie, P. Polarized Photoluminescence Excitation Spectroscopy of Single-Walled Carbon Nanotubes. *Phys. Rev. Lett.* **2007**, *98*, 167406.
70. Kato, T.; Hatakeyama, R. Exciton Energy Transfer-Assisted Photoluminescence Brightening from Freestanding Single-Walled Carbon Nanotube Bundles. *J. Am. Chem. Soc.* **2008**, *130*, 8101–8107.
71. Qian, H.; Georgi, C.; Anderson, N.; Green, A. A.; Hersam, M. C.; Novotny, L.; Hartschuh, A. Exciton Energy Transfer in Pairs of Single-Walled Carbon Nanotubes. *Nano Lett.* **2008**, *8*, 1363–1367.
72. Han, J. H.; Paulus, G. L. C.; Maruyama, R.; Heller, D. A.; Kim, W. J.; Barone, P. W.; Lee, C. Y.; Choi, J. H.; Ham, M. H.; Song, C.; *et al.* Exciton Antennas and Concentrators from Core−Shell and Corrugated Carbon Nanotube Filaments of Homogeneous Composition. *Nat. Mater.* **2010**, *9*, 833–839.
73. Torrens, O. N.; Zheng, M.; Kikkawa, J. M. Energy of K-Momentum Dark Excitons in Carbon Nanotubes by Optical Spectroscopy. *Phys. Rev. Lett.* **2008**, *101*, 157401.
74. O'Connell, M. J.; Bachilo, S. M.; Huffman, C. B.; Moore, V. C.; Strano, M. S.; Haroz, E. H.; Rialon, K. L.; Boul, P. J.; Noon, W. H.; Kittrell, C.; *et al.* Band Gap Fluorescence from Individual Single-Walled Carbon Nanotubes. *Science* **2002**, *297*, 593–596.
75. Weisman, R. B.; Bachilo, S. M. Dependence of Optical Transition Energies on Structure for Single-Walled Carbon Nanotubes in Aqueous Suspension: An Empirical Kataura Plot. *Nano Lett.* **2003**, *3*, 1235.
76. Liu, K.; Deslippe, J.; Xiao, F.; Capaz, R. B.; Hong, X.; Aloni, S.; Zettl, A.; Wang, W.; Bai, X.; Louie, S. G.; *et al.* An Atlas of Carbon Nanotube Optical Transitions. *Nat. Nanotechnol.* **2012**, *7*, 325–329.
77. Bernath, P. F. The Spectroscopy of Water Vapour: Experiment, Theory and Applications. *Phys. Chem. Chem. Phys.* **2002**, *4*, 1501–1509.
78. O'Connell, M. J.; Eibergen, E. E.; Doorn, S. K. Chiral Selectivity in the Charge-Transfer Bleaching of Singlewalled Carbon-Nanotube Spectra. *Nat. Mater.* **2005**, *4*, 412–418.
79. Ge, C.; Du, J.; Zhao, L.; Wang, L.; Liu, Y.; Li, D.; Yang, Y.; Zhou, R.; Zhao, Y.; Chai, Z. Binding of Blood Proteins to Carbon Nanotubes Reduces Cytotoxicity. *Proc. Natl. Acad. Sci. U.S.A.* **2011**, *108*, 16968–16973.
80. Tu, X.; Manohar, S.; Jagota, A.; Zheng, M. DNA Sequence Motifs for Structure-Specific Recognition and Separation of Carbon Nanotubes. *Nature* **2009**, *460*, 250–253.
81. Zhao, X.; Liu, R.; Chi, Z.; Teng, Y.; Qin, P. New Insights into the Behavior of Bovine Serum Albumin Adsorbed onto Carbon Nanotubes: Comprehensive Spectroscopic Studies. *J. Phys. Chem. B* **2010**, *114*, 5625–5631.
82. Hartmann, G. The Structure and Action of Proteins. *Angew. Chem.* **1970**, *82*, 780.
83. Kerr, J. C.; Huang, Y. Y.; Marshall, J. E.; Terentjev, E. M. Effect of Filament Aspect Ratio on the Dielectric Response of Multiwalled Carbon Nanotube Composites. *J. Appl. Phys.* **2011**, *109*, 094109.

84. Smoluchowski, M. Classe des Sciences Math. et Naturelles. *Bull. Int. Acad. Sci. Cracovie* **1903**, 182–199.
85. Lumpkin, O. J.; Dijardin, P.; Zimm, B. H. Theory of Gel Electrophoresis of DNA. *Biopolymers* **1985**, *24*, 1573–1593.
86. Ge, S.; Ken, K.; Atsushi, T.; Tisato, K. Bovine Serum Albumin Adsorption onto Immobilized Organotrichlorosilane Surface: Influence of the Phase Separation on Protein Adsorption Patterns. *J. Biomater. Sci., Polym. Ed.* **1998**, *9*, 131–150.
87. Allison, S. A.; Wang, H.; Laue, T. M.; Wilson, T. J.; Wooll, J. O. Visualizing Ion Relaxation in the Transport of Short DNA Fragments. *Biophys. J.* **1999**, *76*, 2488–2501.
88. Storm, A. J.; Storm, C.; Chen, J.; Zandbergen, H.; Joanny, J.-F.; Dekker, C.; Fast, D. N. A. Translocation through a Solid-State Nanopore. *Nano Lett.* **2005**, *5*, 1193–1197.
89. Benedict, L. X.; Louie, S. G.; Cohen, M. L. Static Polarizabilities of Single-Wall Carbon Nanotubes. *Phys. Rev. B* **1995**, *52*, 8541.
90. Brothers, E. N.; Izmaylov, A. F.; Scuseria, G. F.; Kudin, K. N. Analytically Calculated Polarizability of Carbon Nanotubes: Single Wall, Co-axial, and Bundled Systems. *J. Phys. Chem. C* **2008**, *112*, 1396–1400.